

Scattering of one-dimensional quantum droplets by a reflectionless potential well

Xiaoxiao Hu ¹, Zhiqiang Li,¹ Yu Guo ², Yajiang Chen ¹ and Xiaobing Luo ^{1,3,*}

¹*Department of Physics, Zhejiang Sci-Tech University, Hangzhou 310018, China*

²*Hunan Provincial Key Laboratory of Flexible Electronic Materials Genome Engineering, School of Physics and Electronic Science, Changsha University of Science and Technology, Changsha 410114, China*

³*School of Mathematics and Physics, Jinggangshan University, Ji'an 343009, China*



(Received 23 May 2023; accepted 11 October 2023; published 3 November 2023)

We investigate both analytically and numerically the scattering of one-dimensional quantum droplets by a Pöschl-Teller reflectionless potential well, confirming that there is a sharp transition between full reflection and full transmission at a certain critical incident speed for both small droplets and large flat-top droplets. We observe sharp differences between small quantum droplet scattering and large quantum droplet scattering. The scattering of small quantum droplets is similar to that of solitons, where a spatially symmetric trapped mode is formed at the critical speed, whereas for large quantum droplets a spatially asymmetric trapped mode is formed. Additionally, a nonmonotonic dependence of the critical speed on the atom number is identified: On the small-droplet side, the critical speed increases with the atom number, while in the flat-top regime, the critical speed decreases with increasing atom number. Strikingly, the scattering excites internal modes below the particle-emission threshold, preventing the quantum droplets from emitting radiation upon interaction with the potential. Analysis of the small-amplitude excitation spectrum shows that as the number of particles increases, it becomes increasingly difficult to emit particles out of the droplet during scattering, while radiation from solitons cannot be completely avoided. Finally, we study the collision of two quantum droplets at the reflectionless potential, revealing the role of the π -phase difference generator played by the reflectionless potential.

DOI: [10.1103/PhysRevA.108.053306](https://doi.org/10.1103/PhysRevA.108.053306)

I. INTRODUCTION

van der Waals theory shows that at high densities the liquid state is created by a balance of interatomic attraction and short-range repulsion. However, quantum droplet generation in ultracold and very dilute atomic gases does not follow this classical liquid concept [1–12], and the generation of quantum droplets is purely a manifestation of quantum nature, where the competition between mean-field (MF) interactions and beyond-mean-field (BMF) corrections leads to stabilization of the system in self-bound droplet states [13]. The BMF contribution accounts for the leading correction to the ground-state energy for a weakly interacting Bose gas [14,15], pioneered by Lee, Huang, and Yang [16], which stabilizes the gas to prevent collapse due to MF effects, hence termed the Lee-Huang-Yang (LHY) correction. The new type of self-bound quantum liquid states has been realized experimentally in short-range interacting homonuclear [1–3] and heteronuclear [4,5] bosonic mixtures and in dipolar gases [6–12], manifesting the crucial role played by the BMF quantum fluctuation (see recent reviews in [17–19] and references therein). Focusing on short-range interacting droplets, theoretical and experimental studies have been carried out on their dynamical formation [2,20,21], the crossover from droplet to gaseous Bose-Einstein condensate [3,22,23], higher-order quantum and thermal fluctuations [24,25], and collision dynamics [26].

The dimensional crossover for the BMF correction in Bose gases has also been analyzed in detail [27–29]. The BMF contribution comes from the zero-point energy of all Bogoliubov modes, which is heavily dependent on the density of states and thus on the dimensionality of the system. Correspondingly, the sign and the structure of the BMF terms differ in the different dimensional geometries [30]. One-dimensional (1D) droplets, governed by attractive LHY corrections, differ fundamentally from 3D and 2D droplets (with repulsive LHY corrections) [30]. In particular, the stability of 1D quantum droplets has significant advantages, as the three-body loss in a 1D droplet is greatly reduced compared to its 3D counterpart [27,31]. To date, within the framework of the modified Gross-Pitaevskii equation [30,32,33], the behaviors of 1D quantum droplets, such as collective excitations and dynamics [34–37], confinement [38,39], the effects of Rabi [40] or spin-orbit couplings [41,42], and nonequilibrium properties [43], have been extensively studied. Interestingly, however, scattering of one-dimensional quantum droplets remains largely unexplored [44].

One of the most fascinating phenomena of bright solitons that occurs in nonautonomous nonlinear systems is quantum reflection, which portrays the wave nature of solitons when scattered by surfaces or steps [45–48], potential barriers [49–55], potential wells [56–61], and impurities [62–67]. Experimentally, potential wells (barriers) can be created by illuminating a condensate with a red (blue)-detuned laser beam. So far, experiments have reported reflections of solitons from potential wells [68], reflections from barriers [69], and

*Corresponding author: xiaobingluo2013@aliyun.com

the use of narrow barrier-splitting solitons for the design of soliton interferometers [70]. The wave-particle duality of the soliton makes it possible for the soliton to undergo a quantum reflection from an attractive potential well and yet still retain its particlelike integrity to a large extent [58]. In such a phenomenon, even without classical turning points, quantum reflection may occur as the soliton approaches the potential, which can be understood by the formation of a trapped mode at the center of potential [59,61,65]. A well-known example is the bright soliton of the nonlinear Schrödinger equation (NLSE) scattering from the Pöschl-Teller reflectionless potential well [58,60,61]. In the case of solitons scattering from the reflectionless potential, quantum reflection occurs only below a critical initial speed, with a sharp transition between quantum reflection and transmission. An accurate calculation of the critical speed has been proposed by determining the profile and energy of the trapped mode using a variational method with an ansatz of a soliton whose density profile is spatially symmetric with respect to the potential center. Such studies enabled the understanding of the mechanism of soliton energy exchange during scattering and will help in the implementation of future all-optical technologies such as soliton diodes and logic gates [71–73]. One-dimensional quantum droplets, as macroscopic manifestations of quantum fluctuations, are predicted to exhibit a number of appealing properties, such as collisional features, collective excitations, and shapes (e.g., a liquidlike incompressible phase with a flat-top density profile, highlighted by a uniform bulk density, appears at large particle numbers), which are fundamentally different from those of one-dimensional bright solitons. Given the striking differences in the properties of solitons and droplets, it is natural to ask the following questions of general interest regarding the scattering of quantum droplets from the reflectionless potential: Does the sharp transition from quantum reflection to full transmission also occur in the scattering of quantum droplets, as it does in the scattering of bright solitons of the NLSE? If yes, what are the unconventional features in quantum droplet scattering?

In the present work, we comprehensively study the scattering of quantum droplets by the Pöschl-Teller reflectionless potential well. We confirm that quantum reflection occurs, with a sharp transition between full reflection and full transmission at a critical initial speed, both for small droplets with a sech² shape and for large droplets with a broad flat-top plateau. Our study shows that quantum droplets can be either completely reflected or completely transmitted off the reflectionless potential without any splitting or particle emission. The 100% reflectivity or 100% transmittance without any radiation when interacting with the reflectionless potential is a peculiar feature of quantum droplets, which is not really accessible to the scattering of solitons (especially large solitons). Our numerical simulations show that the trapped mode (i.e., full trapping by the potential at the critical speed) of the quantum droplets turns out to be spatially asymmetric at large particle numbers, which differs from the counterpart of small quantum droplets and solitons and can be captured by a variational method with a position-dependent trial wave function. We also precisely determine the critical speeds for the quantum reflection of the droplet, showing a different dependence of the critical speed on the atom number for

small and large droplets, and explain why the quantum droplet experiences no radiation or particle loss during scattering by analyzing the collective excitations of the quantum droplet.

The rest of the paper is organized as follows. In Sec. II we give the exact solution of quantum droplets in free space and discuss the properties of quantum droplets in the two limits of large and small atom numbers. In Sec. III we define the reflection and transmission coefficients and study the scattering of quantum droplets numerically. In Sec. IV we use three methods to calculate the critical speed below which quantum reflection occurs and analyze the formation of the unbalanced trapped modes (the nonlinear single-node stationary states) of the large quantum droplets with a flat-top density profile. In Sec. V we analyze the collective excitations during the scattering of quantum droplets. In Sec. VI we study the collisions between two quantum droplets at the Pöschl-Teller reflectionless potential well. We summarize and discuss our main findings in Sec. VII.

II. SOLUTIONS OF QUANTUM DROPLETS

We consider a two-component Bose-Bose mixture with equal mass symmetry, with mutual repulsion between atoms of the same component $g_{\uparrow\uparrow} = g_{\downarrow\downarrow} = g_0 > 0$, with mutual attraction between atoms of different components $g_{\uparrow\downarrow} < 0$ and an equal number of particles of both components $N_{\uparrow} = N_{\downarrow} = \tilde{N}/2$. Near the MF collapse point ($\delta g = g_{\uparrow\downarrow} + \sqrt{g_{\uparrow\uparrow}g_{\downarrow\downarrow}} \ll g_0$), the energy of the homogeneous mixture can be found and the Gross-Pitaevskii equation (GPE) is derived as [30,34,36]

$$i\hbar \frac{\partial \Psi(x, t)}{\partial t} = -\frac{\hbar^2}{2m} \frac{\partial^2 \Psi(x, t)}{\partial x^2} + \frac{\delta g}{2} |\Psi(x, t)|^2 \Psi(x, t) - \frac{\sqrt{m}}{\pi \hbar} g_0^{3/2} |\Psi(x, t)| \Psi(x, t), \quad (1)$$

with total atom number $\tilde{N} = \int_{-\infty}^{\infty} |\Psi(x)|^2 dx$, where the last term on the right-hand side of Eq. (1) corresponds to the LHY term, which is the first-order BMF correction term accounting for the quantum many-body effect in the weakly interacting regime ($g_0/n \ll 1$, where n is the total density of the component). In experiments, it is possible to tune δg to positive and negative values. Here we define the relative change of the mean-field intensity $g = \delta g / \delta g_0$ (where $\delta g_0 > 0$ is a constant) to discuss a more general solution of Eq. (1). By defining the length $\xi_0 = \frac{\pi \hbar^2 \delta g_0^{1/2}}{2m g_0^{3/2}}$, the time $t_0 = \frac{\pi^2 \hbar^3 \delta g_0}{4m g_0^3}$, and the energy $E_0 = \frac{4m g_0^3}{\pi^2 \hbar^2 \delta g_0}$ as the characteristic units, Eq. (1) can be written in a dimensionless form

$$i\psi_t = -\frac{1}{2} \psi_{xx} + g |\psi|^2 \psi - |\psi| \psi, \quad (2)$$

with the norm defined by $N = \int_{-\infty}^{\infty} |\psi(x)|^2 dx = \frac{\pi \tilde{N}}{2} (\delta g_0 / g_0)^{3/2}$. Regardless of the sign of g , the attractive BMF term allows the system to admit a self-bound ground state [30,36] in the form of $\psi(x, t) = \psi_0(x) e^{-i\mu t}$, with

$$\psi_0(x) = \frac{-3\mu}{1 + \sqrt{1 + \frac{9\mu g}{2} \cosh(\sqrt{-2\mu} x^2)}}. \quad (3)$$

The relation between the chemical potential μ and norm N of the droplet depends on the sign of g and is given by

$$N_{g=0} = 3\sqrt{2}(-\mu)^{3/2}, \quad (4)$$

$$N_{g<0} = n_0 \sqrt{\frac{2}{\mu_0}} \left(\sqrt{\frac{-\mu}{\mu_0}} - \arctan \sqrt{\frac{-\mu}{\mu_0}} \right), \quad (5)$$

$$N_{g>0} = n_0 \sqrt{-\frac{2}{\mu_0}} \left(\ln \frac{1 + \sqrt{\mu/\mu_0}}{\sqrt{1 - \mu/\mu_0}} - \sqrt{\frac{\mu}{\mu_0}} \right). \quad (6)$$

In Eqs. (5) and (6), $\mu_0 = -2/9g$ and $n_0 = 4/9g^2$ are the chemical potential and the saturation density of a spatially uniform liquid at $g > 0$, respectively. When $g = 0$, Eq. (3) represents the known Korteweg–de Vries (KdV)-type droplet solution

$$\psi_0(x) = \frac{-3\mu}{2} \operatorname{sech}^2 \left(\sqrt{\frac{-\mu}{2}} x \right). \quad (7)$$

In our work, we focus on the $g > 0$ case. The first thing we need to understand is the nature of the free quantum droplet solution when $g > 0$. It is worth noting that for $g > 0$, $0 \leq \sqrt{1 + \frac{9\mu g}{2}} < 1$ in Eq. (3), the characteristics of quantum droplets can be analyzed using the formula $\tanh(a + X) + \tanh(a - X) = \frac{2 \tanh(2a)}{1 + \operatorname{sech}(2a) \cosh(2X)}$, by which the ground-state solution of the droplet can be written as

$$\psi_0(x) = \sqrt{A} [\tanh(a + \sqrt{A}gx) + \tanh(a - \sqrt{A}gx)], \quad (8)$$

where

$$A = \frac{-\mu}{2g}, \quad (9)$$

$$a = \frac{1}{2} \operatorname{arctanh} \left[\left(-\frac{9}{2} \mu g \right)^{1/2} \right]. \quad (10)$$

From Eqs. (6) and (10) we have $\mu(N \rightarrow \infty) = -\frac{2}{9g}$, $\mu(N \rightarrow 0) = 0$, $-\frac{2}{9} < \mu g < 0$, and $a \in (0, \infty)$, which increases with N . For a large quantum droplet, which corresponds to a large value of a , Eq. (8) gives rise to the wave function of large-size droplets characterized by the kink structures at the edges as well as a uniform flat-top structure in the middle,

$$\psi_{\text{middle}} = 2\sqrt{A}, \quad (11)$$

$$\psi_{\text{kink}} = \sqrt{A} \left[\tanh \left(a \mp \sqrt{\frac{-\mu}{2}} x \right) + 1 \right]. \quad (12)$$

For quantum droplets with a small value of a ($a \ll 1$), the solution (8) can be approximated by Taylor expansion as

$$\psi_0(x) \approx 2a\sqrt{A} \operatorname{sech}^2 \left(\sqrt{\frac{-\mu}{2}} x \right), \quad (13)$$

which is found to feature a similar density profile to the KdV-type droplets.

We show analytically that, upon variation of a (which vanishes when $g = 0$), two physically distinct regimes, small droplets of sech^2 shape and large droplets with a flat-top plateau, can be identified. From the analytical expressions (11)–(13), we observe sharp differences between the sech^2 -shaped and flat-top droplets. It can be seen that for small

droplets with $a \ll 1$, as $\sqrt{-\mu/2}$ grows with N , the width of the sech^2 -shaped droplets becomes narrower and they behave like bright solitons. In contrast, for large quantum droplets with $a \gg 1$, the MF term repulsion effect becomes significant, leading to the separation of kink and antikink pairs and thus to the formation of kink structures at the edges and flat-top structures in the center. In this case, the width of flat-top droplets will instead increase with the norm N , which is similar to the classical liquid, where a plateau in the density profile expands with the growth of the mass of the droplet.

III. SCATTERING OF QUANTUM DROPLETS

In the preceding section we explored analytically the ground states of a one-dimensional free-space quantum droplet system, and in this section we consider the scattering of strictly one-dimensional quantum droplets by a reflectionless Pöschl-Teller attractive potential $V(x) = -U_0 \operatorname{sech}^2(\alpha x)$ ($\alpha = \sqrt{U_0}$ is necessary for reflectionless scattering of linear matter waves), whose dynamics is governed by the GPE containing the external potential

$$i\psi_t = -\frac{1}{2}\psi_{xx} + g|\psi|^2\psi - |\psi|\psi - U_0 \operatorname{sech}^2(\alpha x)\psi, \quad (14)$$

where U_0 is expressed in units of E_0 . Note that δg_0 is an arbitrary constant used as a measure. In this paper we choose $g = 0$ (corresponding to $\delta g = 0$) and $g = \pm 1$ by assuming $\delta g_0 = |\delta g|$ so that the droplet properties can only be controlled by the rescaled norm N together with the sign of g . Due to the invariance of the system under Galilean transformations, the exact movable quantum droplet solution of the dimensionless GPE (2) can be obtained from the stationary solution as

$$\psi(x, t) = \frac{-3\mu e^{i[(x-\tilde{x}_0)v+(v^2/2)t-\mu t]}}{1 + \sqrt{1 + \frac{9\mu g}{2} \cosh[\sqrt{-2\mu}(x - \tilde{x}_0)^2]}}, \quad (15)$$

where v and \tilde{x}_0 are the initial speed and initial position of the quantum droplet, respectively. We study the scattering of quantum droplets by numerically solving Eq. (14) with $\psi(x, 0)$ in Eq. (15) as the initial profile, based on the split-step Fourier (SSF) method. To get started, we define the corresponding reflection (R) and transmission (T) coefficients as

$$R = (1/N) \int_{-\infty}^{-l} |\psi(x, t_f)|^2 dx, \quad (16)$$

$$T = (1/N) \int_l^{\infty} |\psi(x, t_f)|^2 dx, \quad (17)$$

where l is the length greater than the width of the potential well and t_f is the evolution time needed to make the scattered quantum droplets sufficiently distant from the potential well.

Figure 1 shows the numerical results of reflection (red dashed lines) and transmission (blue solid lines) coefficients versus the initial speed of a quantum droplet scattered by the reflectionless attractive potential. It can be seen that there is a sharp transition between full transmission and full reflection with a well-defined critical speed for both large and small quantum droplets. This is directly demonstrated by the spatiotemporal density plots of quantum droplets for two different norms $N = 1$ [Figs. 2(a)–2(c)] and $N = 10$ [Figs. 2(d)–2(f)], where two main outcomes of the scattering are distinguished, depending on the incident speeds. When the incident speed

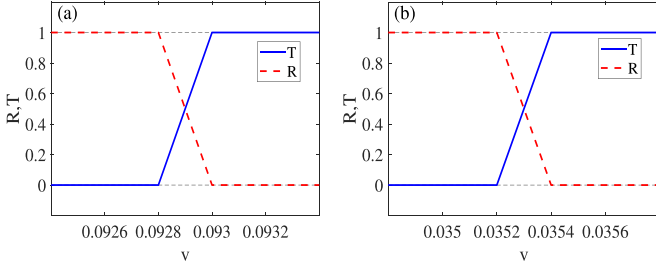


FIG. 1. Reflectance (red dashed line) and transmittance (blue solid line) versus the initial speed of a quantum droplet scattering by a reflectionless potential for (a) a small quantum droplet with $N = 1$ and (b) a large quantum droplet with $N = 10$. The other parameters are $U_0 = 4$, $\alpha = \sqrt{U_0}$, $g = 1$, and $\bar{x}_0 = -30$. Quantities plotted in all the figures are dimensionless.

is below the critical speed, the quantum droplet experiences nonclassical full reflection. The critical speed is then found numerically by increasing the incident speed until the duration of the quantum droplet trapped by the potential reaches the maximum length. When the incident speed exceeds the critical speed, the quantum droplet gets fully transmitted. Importantly, there is a striking difference in the trapped modes between the small and large droplets. The trapped modes of large droplets are found to be spatially asymmetric with respect to the center of the potential, which contrasts with the counterparts of small droplets. Another exotic property is that although the large flat-top droplet can be very wide, it scatters from the potential well without any splitting or radiation, so reflectance and transmittance can reach 100%.

In Fig. 3 we present the phase evolution of the small droplet [Fig. 3(a)] and the large droplet [Fig. 3(b)], corresponding to the density evolution in Figs. 2(b) and 2(e) at the incident speed close to the critical speed, where the quantum droplets are fully trapped by the potential for a long time period during the scattering process. In both the small- and large-droplet cases, the phase evolution shows that a significant phase step close to π appears at density dips, as the quantum droplets develop a single-node density distribution during the scattering process. As we will see later, the phase jump of π across the density dip plays an important role in the analysis of the quantum droplet scattering.

IV. CRITICAL MODES IN THE QUANTUM DROPLET SCATTERING PROCESS

The occurrence of quantum reflections indicates the existence of a zero-speed state during scattering, which represents the instantaneous state of the turning point of quantum reflection. Here we define the state of $v(x = x_0) = 0$ (the velocity turning point) during the quantum reflection as the zero-speed state $\phi(x - x_0)$ (where x_0 is the position of droplet peak at the velocity turning point). The energy E_z of the zero-speed state can be calculated from the energy functional

$$E_z(x_0) = \int_{-\infty}^{+\infty} \left[\frac{1}{2} |\phi_x|^2 + \frac{g}{2} |\phi|^4 - \frac{2}{3} |\phi|^3 + V(x) |\phi|^2 \right] dx. \quad (18)$$

As the quantum droplet is initially far away from the potential well, the potential energy is very small and negligible. Thus, the initial energy of the quantum droplet, calculated from Eq. (14) with the initial profile $\psi(x, 0)$, can be given by

$$\begin{aligned} E_d &= \int_{-\infty}^{+\infty} \left(\frac{1}{2} |\psi_x|^2 + \frac{g}{2} |\psi|^4 - \frac{2}{3} |\psi|^3 \right) dx \\ &= \frac{1}{2} N v^2 + \int_{-\infty}^{+\infty} \left(\frac{1}{2} |(\psi_0)_x|^2 + \frac{g}{2} |\psi_0|^4 - \frac{2}{3} |\psi_0|^3 \right) dx \\ &= \frac{1}{2} N v^2 + E_{sd}, \end{aligned} \quad (19)$$

where E_{sd} is the energy of the stationary droplet in the form of Eq. (3). Given a droplet in free space with an initial speed v , its quantum reflection occurs at the position where the droplet energy in the reflectionless potential equals the initial energy. Energy conservation relates these energies as

$$E_z(x_0) = \frac{1}{2} N v^2 + E_{sd}. \quad (20)$$

The energy of the zero-speed state is increased with the initial speed of the droplet. It reaches a maximum value at the critical speed, above which the droplet gets transmitted. Thus, the critical speed can be computed numerically by increasing the initial droplet speed such that the zero-speed state of maximum energy can be reached. Analytically, the critical speed can be derived from Eq. (20) as

$$v_c = \sqrt{\frac{2[(E_z)_{\max} - E_{sd}]}{N}}, \quad (21)$$

where $(E_z)_{\max}$ stands for the maximum value of $E_z(x_0)$. Quantum droplets with different initial speeds produce different zero-speed states at different locations during quantum reflection. To describe the zero-speed state at different positions, we propose the position-dependent trial function

$$\phi(x) = A \psi_0[\gamma(x - x_0)] \tanh(\beta x), \quad (22)$$

where γ and β are the variational parameters, with β accounting for the central slope and γ the overall width of the mode, and x_0 denotes the position of the zero-speed state. Here the choice of the trial wave function (22) with a node given by $\tanh(x)$ is justified by this phase jump of π as illustrated in the phase plot of Fig. 3. We normalize the trial function to N , yielding

$$A(\gamma, \beta, x_0) = \left(\frac{N}{\int_{-\infty}^{+\infty} |\psi_0[\gamma(x - x_0)] \tanh(\beta x)|^2 dx} \right)^{1/2}. \quad (23)$$

The energy functional for the zero-speed state can be calculated by substituting the normalized trial function (22) into Eq. (18). However, the integration cannot be obtained in analytical form. Thus, we make the integral in Eq. (23) and the similar integral in the energy functional (18) be computed numerically in terms of γ and β . By plotting $E_z[\gamma, \beta]$ for specific values of N , g , x_0 , and U_0 , the results show that $E_z[\gamma, \beta]$ has a local minimum at $\gamma = \gamma^*$ and $\beta = \beta^*$. The minimum energy $E_z[\gamma^*, \beta^*]$ obtained in this way is supposed to be the energy of the zero-speed state at x_0 . Substituting $E_z = E_z[\gamma^*, \beta^*]$ into Eq. (20), we can get the initial speed

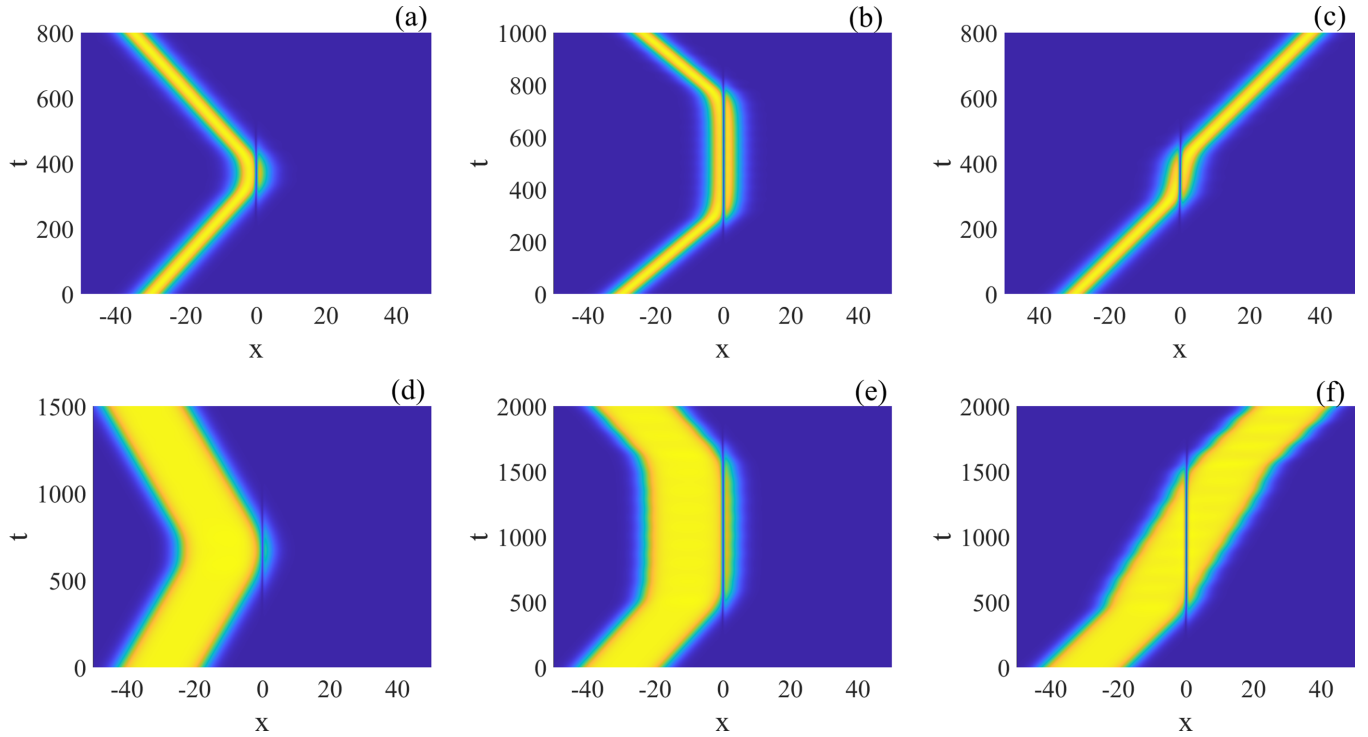


FIG. 2. Scattering of quantum droplets at different speeds by a reflectionless potential centered at $x = 0$ for (a)–(c) small quantum droplets ($N = 1$) and (d)–(f) large quantum droplets ($N = 10$). The initial speeds of the quantum droplets are (a) $v = 0.08$, (b) $v = v_c \approx 0.0928757$, (c) $v = 0.095$, (d) $v = 0.03$, (e) $v = v_c \approx 0.03532$, and (f) $v = 0.04$. The other parameters are $U_0 = 4$, $\alpha = \sqrt{U_0}$, $g = 1$, and $\tilde{x}_0 = -30$.

that produces a zero-speed state at the given position x_0 in the quantum reflection process. According to Eq. (21), the energy $E_z[\gamma^*, \beta^*]$ maximum in terms of x_0 gives the critical speed above which transmission occurs. A similar but position-independent variational solution has been used to accurately predict the critical speed between reflection and transmission of bright solitons in the reflectionless potential [61].

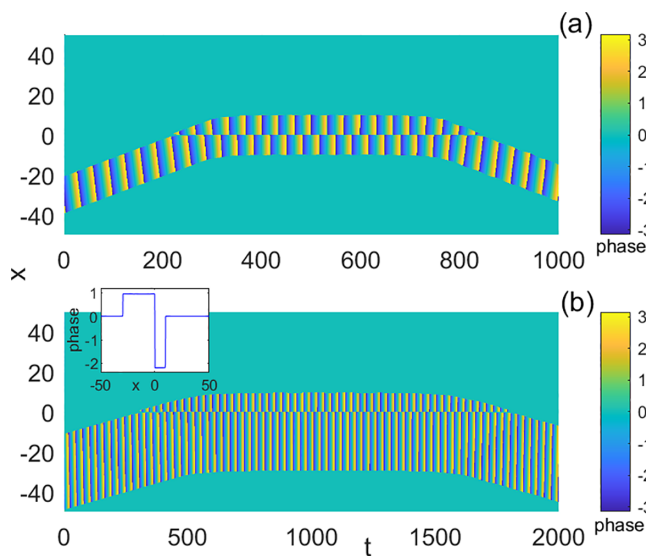


FIG. 3. Phase evolution of (a) the small droplet and (b) the large droplet at $v \approx v_c$, corresponding to the density evolution as in Figs. 2(b) and 2(e), respectively.

In Fig. 4 we plot the energy of zero-speed state versus x_0 using the variational method with the trial function (22). Figure 4 shows that the energy of the zero-speed state does indeed have a maximum at certain values of x_0 . Substituting these maximum energy values into Eq. (21) yields the critical speed. The energy of zero-speed states exhibits left-right symmetry, because the quantum droplet can be launched from either the left or the right. The zero-speed states with maximum energy with respect to x_0 are also called trapped modes, because at the critical speed the quantum droplet remains inside the potential indefinitely during scattering. Since these trapped modes have an energy functional corresponding to a maximum rather than a minimum with respect to x_0 , they are unstable against small perturbations in their position. If the speed of the incident droplet is slightly shifted from the critical speed, a trapped mode is temporarily formed during the scattering process and a quantum droplet is then ejected from the potential and gets fully transmitted or reflected. This instability explains the sharpness of the transition between full transmission and full reflection. The duration of the trapped mode increases as the initial speed gets closer to the critical speed. As observed in Figs. 2(b) and 2(e), when $v \approx v_c$, the droplet can be completely trapped by the potential for a considerably long time. If initially prepared with precision, the trapped mode can exist for an indefinitely long period of time in the absence of any external and computational perturbations, thus representing an exact nonlinear eigenstate of the system.

As can be seen from Figs. 4(a) and 4(b), for small quantum droplets, the energy maximum is at the center of the potential $x_0 = 0$, while for large quantum droplets the

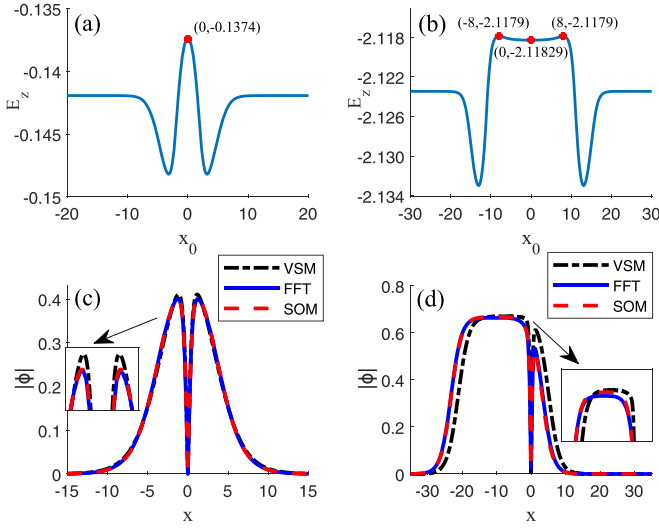


FIG. 4. Dependence of the energy of zero-speed states on position x_0 derived from the variational method using the position-dependent trial function (22) for (a) a small quantum droplet ($N = 1$) and (b) a large quantum droplet ($N = 10$). The other parameters are $U_0 = 4$ and $g = 1$. The energy maxima with respect to x_0 , marked by red dots, represent the trapped modes corresponding to the nonlinear single-node stationary states of the governing GPE (14). Also shown are the profiles of the trapped modes: (c) the unstable symmetric trapped mode corresponding to the point $(0, -0.1374)$, as shown in (a), and (d) the unstable asymmetric trapped mode corresponding to the point $(-8, -2.1179)$, as shown in (b).

maximum-energy point is displaced from the center of the potential. The trapped mode, corresponding to an energy maximum in terms of x_0 , can be obtained for the small and large quantum droplets by using three numerical methods, as shown in Figs. 4(c) and 4(d). Our first numerical procedure to calculate the trapped mode starts by solving Eq. (14) using the SSF method, where the incident droplet speed is adjusted until the droplet is trapped in the potential for a substantial amount of time. The variational method (VM) is the second method of calculating the trapped mode based on the trial wave function (22) as described in detail at the beginning of this section, and the third method involves calculating the nonlinear stationary state of Eq. (14) using a square operator method (SOM) [74]. As can be seen in Figs. 4(c) and 4(d), the trapped mode profiles obtained by the three methods are basically identical. For the small solitonlike droplet, the trapped mode has a symmetric shape as shown in Fig. 4(c), whereas the trapped mode of the large quantum droplet has an asymmetric density profile as shown in Fig. 4(d). Inspections also show that the profile of the asymmetric trapped mode for the large droplet obtained by VM is not as accurate as that obtained by the SSF method and the SOM.

Once the trapped mode and its energy have been determined, we can calculate the critical speed by means of Eq. (21). In Table I we list the numerical values of the critical droplet speed calculated by these three numerical methods. A good match can clearly be seen in the table.

In Fig. 4(b) we are surprised to find that there is a local energy minimum at $x_0 = 0$ for a large quantum droplet, corresponding to a stable spatially symmetric eigenstate of

TABLE I. Three methods to solve the critical speed.

N	Critical speed v_c		
	SSF	VM	SOM
0.1	0.0568	0.059008912	0.0567048776
0.3	0.0811	0.075073377	0.0811317970
0.5	0.0900	0.089720945	0.0899700200
0.6	0.0921	0.095240699	0.0920241325
0.8	0.0935	0.096590948	0.0935224949
1	0.0928	0.095695377	0.0928252791
2	0.078	0.080108024	0.0784391394
4	0.055	0.053647658	0.0555275841
6	0.045	0.043133578	0.0453212798
8	0.039	0.037331779	0.0390179123
10	0.035	0.033341549	0.0351731171
12	0.031	0.030435107	0.0312519825
14	0.029	0.028031223	0.0290528706
16	0.027	0.026326940	0.0273519847

the governing GPE (14). However, its energy is lower than the energy of the unstable trapped mode. This suggests that when a large quantum droplet is scattered by the reflectionless potential at the critical speed, an unstable asymmetric trapped mode is excited instead of the stable symmetric nonlinear eigenmode. For initial speeds above the critical speed, the energy of the incoming droplet is large enough to pass through the potential and thus the large droplet is not trapped in the symmetric eigenmode of the nonlinear system. To confirm the stable spatially symmetric eigenmode of the large droplet predicted by the variational method, we first numerically obtain the symmetric stationary mode of Eq. (14) by the square operator iteration method using the variational solution as the initial seed and then give the propagation of the symmetric stationary mode, which is invariant with time as expected, as illustrated in Fig. 5(a). By imposing the symmetric stationary mode with a low initial speed, as seen in Fig. 5(b), the propagation simulation shows that this state oscillates back and forth around the equilibrium point $x = 0$ and neither reflection nor transmission occurs, as its energy is lower than the two peaks marked by red dots in Fig. 4(b). This further validates the stability of such a symmetric eigenmode for large flat-top

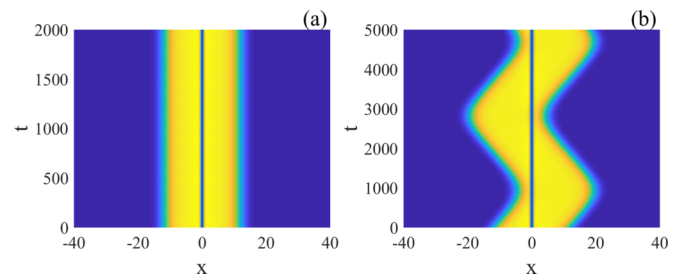


FIG. 5. (a) Top view of the spatiotemporal density evolution of the stable symmetric nonlinear stationary state of Eq. (14) obtained by the square operator method, corresponding to the marked point $(0, -2.11829)$ for the large quantum droplet, as shown in Fig. 4(b), obtained by the variational method. (b) Density evolution of the symmetric nonlinear stationary state as shown in (a), with an initial speed $v = 0.01$. The other parameters are $U_0 = 4$ and $g = 1$.

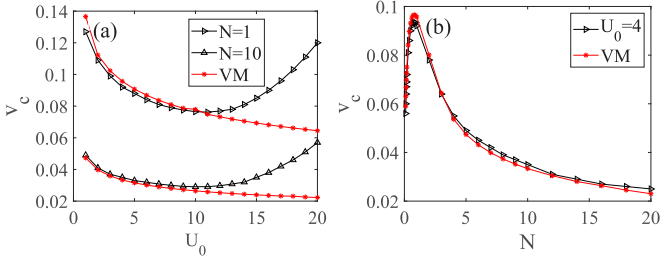


FIG. 6. Critical speed v_c versus (a) potential well depth U_0 and (b) norm N . The black lines with triangles represent the results obtained from the numerical simulation of Eq. (14) using the SSF method and the red lines with asterisks represent the results obtained by the variational method.

quantum droplets. The results of the variational approach also show the existence of zero-speed states with energies lower than the energy of the stationary quantum droplets, as shown by the dips in Figs. 4(a) and 4(b). However, these low-energy states are not excited during the scattering process because the incoming quantum droplets far from the potential have higher energy than these low-energy zero-speed states. The physics of these low-energy states will be discussed in detail elsewhere.

In Fig. 6(a) we report the value of the critical speed as a function of the potential well depth U_0 , comparing the results for small and large N derived from both the VM solution and the exact numerical solution using the SSF method. As expected, the critical speed is well captured by the VM for a wide range of relatively small U_0 (roughly $U_0 < 10$). As the potential well depth increases progressively, the VM becomes inapplicable. Figure 6(b) shows the dependence of the critical speed on the size of the droplet. There is a nonmonotonic dependence, with the largest critical speed reached at $N \approx 1$. For small N , the critical speed increases with the increase of N , which is the same as in the case of bright solitons. However, the dependence of the critical speed of the droplet on the atomic number is reversed when the droplet is in the flat-top regime. It can be seen that for larger N , the critical speed of the droplet decreases with increasing N . This is a unique feature in comparison to the 1D soliton, where the critical speed is only found to increase with N . This peculiarity occurs because of a transition from small droplets with a sech^2 shape to large droplets with a flat-top plateau. A small droplet has an approximately sech^2 shape with decreasing width as N increases, while in the opposite limit, unlike its 1D soliton counterpart, the size of large droplets grows with N . As can be seen in Fig. 6(b), the VM is able to accurately predict the critical speed even for large droplets with flat-top density profiles.

V. COLLECTIVE EXCITATION OF QUANTUM DROPLETS IN THE SCATTERING PROCESS

As is well known, internal modes are linear eigenmodes inherent to stable localized nonlinear states in nonintegrable systems, which are responsible for the internal oscillations of the nonlinear states. Further careful examination of the scattering dynamics shows that the quantum droplet size exhibits extremely small (invisible to the naked eye) internal

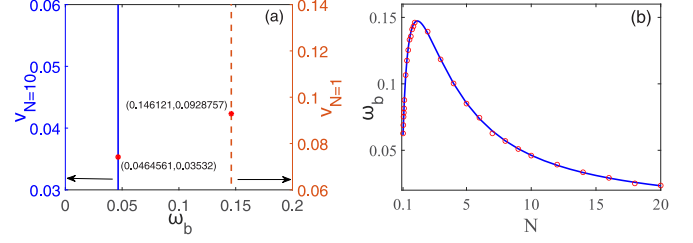


FIG. 7. (a) Initial speed v versus breathing mode frequency ω_b with different norms $N = 1$ (orange dashed line) and $N = 10$ (blue solid line). The red closed circles mark the breathing mode frequencies at the critical speeds for the quantum reflection of the quantum droplets for the cases $N = 1$ and 10. (b) Frequency ω_b versus norm N . The red open circles show the numerically calculated excitation frequency [i.e., the oscillation frequency of $X(t)$] after scattering and the blue solid line is the breathing mode frequency obtained by solving the BdG equation. The other parameters are $U_0 = 4$ and $g = 1$.

oscillations after scattering, which should be responsible for internal mode excitation. The breathing mode is the lowest internal mode which manifests as a periodic oscillation of the quantum droplet size. Deeper insight into the differences between the scattering states of the small and large quantum droplets can be gained by examining the collective excitation frequencies. To determine the frequency ω_b of the breathing mode, we numerically compute the time evolution of the standard deviation $X = \sqrt{\langle (x - \bar{x})^2 \rangle}$, which measures the size of the quantum droplet, and then use frequency spectrum analysis to obtain the oscillation frequency of $X(t)$. In Fig. 7(a) ω_b is plotted as a function of the initial speed for fixed values of $N = 1$ and 10. We observe that the frequency of the breathing mode excited during scattering is independent of the initial speed and that the same breathing mode is excited whether the droplet is fully reflected or transmitted. Figure 7(b) presents the dependence of the resultant breathing mode on the size of droplet. It can be seen that on the small-droplet side the breathing mode frequency increases with N , whereas on the flat-top-droplet side the breathing mode frequency decreases with increasing N .

To further demonstrate that the oscillatory behavior of a quantum droplet scattered from a localized potential is associated with the existence of internal mode, which can be treated as a localized linear excitation connected to the self-bound ground state of Eq. (2), we linearize the GPE (2) around the ground state given by Eq. (3). Writing $\psi(x, t) = e^{-i\mu t} \{ \psi_0(x) + \sum_{\eta} [u_{\eta}(x)e^{-i\omega_{\eta}t} + v_{\eta}^*(x)e^{i\omega_{\eta}^*t}] \}$ and substituting it into Eq. (2), the Bogoliubov-de Gennes (BdG) equation is obtained by linearization,

$$\begin{bmatrix} \mathcal{T} & \mathcal{M} \\ -\mathcal{M} & -\mathcal{T} \end{bmatrix} \begin{bmatrix} u_{\eta}(x) \\ v_{\eta}(x) \end{bmatrix} = \omega_{\eta} \begin{bmatrix} u_{\eta}(x) \\ v_{\eta}(x) \end{bmatrix}, \quad (24)$$

where

$$\begin{aligned} \mathcal{T} &= -\partial_x^2/2 - \mu + 2g\psi_0^2 - \frac{3}{2}\psi_0, \\ \mathcal{M} &= g\psi_0^2 - \frac{1}{2}\psi_0. \end{aligned} \quad (25)$$

We solve Eq. (24) numerically and find that there can be discrete eigenfrequencies ω_{η} , denoted by the integer η , which are associated with the internal dynamics of the matter wave.

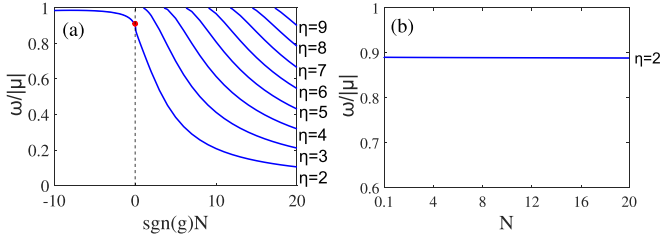


FIG. 8. (a) Ratio of the discrete Bogoliubov frequency ω_η to the particle emission threshold $-\mu$ as a function of $\text{sgn}(g)N$ [where $\text{sgn}(g)$ is the sign of g]. (b) Ratio of the discrete Bogoliubov frequency ω_2 to the particle emission threshold $-\mu$ as a function of N at $g = 0$.

The localized eigenfunctions $[u_\eta(x), v_\eta(x)]^T$, corresponding to real values of ω_η , are known as internal modes of the nonlinear system. The breathing mode with $\eta = 2$ is the lowest nontrivial collective mode in our setup.

The ratio of the discrete Bogoliubov frequencies ω_η to the particle emission threshold $-\mu$ as a function of $\text{sgn}(g)N$ is shown in Fig. 8(a). Here the $\text{sgn}(\delta g)N$ is introduced because the properties of the droplet are governed by the combination of the rescaled atom number N and the sign of δg . The main results of the excitation spectrum are (i) the breathing mode of the quantum droplet ($g > 0$) is always below the particle emission threshold, (ii) there are more internal modes below the particle emission threshold with increasing N for positive g and thus higher internal modes are easily excited

for large quantum droplets, and (iii) the ratio $\omega_\eta/|\mu|$ tends to $+1$ for large negative $\text{sgn}(g)N$ where the droplet crosses over to soliton, indicating that 1D solitons do not sustain small-amplitude collective (internal) modes, but only the continuum spectrum. When $g = 0$, we arrive at a GPE with a rather unusual quadratic-only nonlinearity, where the ratio of the breathing mode frequency to the particle emission threshold is equal to 0.8904, independent of N , as shown in Fig. 8(b). These results have been reported in Ref. [36]. In Fig. 7(b) we compare the breathing mode frequency ω_2 with the oscillation frequency extracted from the periodic oscillation of the droplet width quantified by $X(t)$ and find good agreement between them. This agreement confirms that the scattering of the quantum droplets results in the excitation of the internal mode.

As shown in Fig. 6, when the quantum droplet scatters off a sufficiently deep reflectionless potential, the variational method no longer works. However, even for large potential depth $U_0 = 25$, there is still a sharp transition between full transmission and full (quantum) reflection for both small ($N = 1$) and large ($N = 10$) quantum droplets, as illustrated in Figs. 9(a) and 9(d), respectively. We also examine the spatiotemporal evolution of the density of quantum droplets for the initial speed slightly below [Figs. 9(b) and 9(e)] and above [Figs. 9(c) and 9(f)] the respective critical speeds for small droplets [Figs. 9(b) and 9(c)] and large droplets [Figs. 9(e) and 9(f)]. We observe that the droplets are more excited when the potential well depth is large. Nevertheless, the droplets almost maintain their integrity after scattering. In this case,

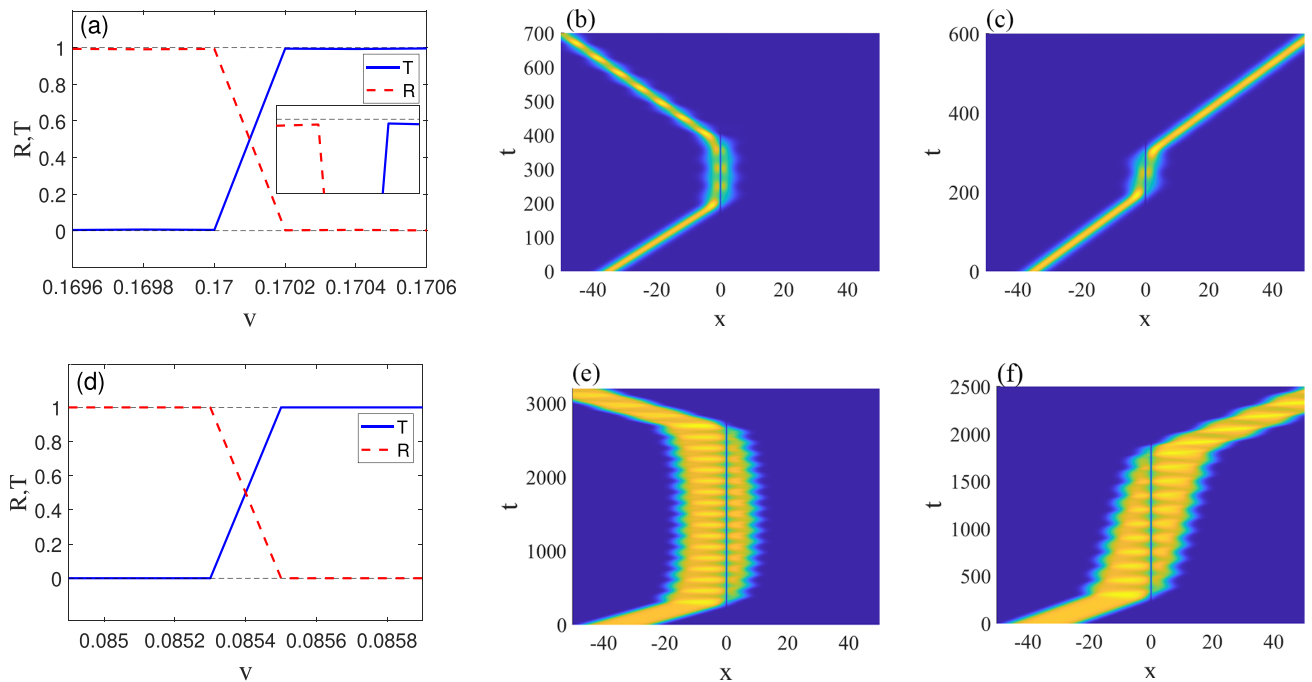


FIG. 9. Scattering of quantum droplets by a reflectionless potential well with a large potential depth for (a)–(c) the small ($N = 1$) and (d)–(f) the large ($N = 10$) quantum droplets: (a) reflectance (red dashed line) and transmittance (blue solid line) versus the initial speed of quantum droplet with $N = 1$, (b) quantum reflection of the small droplet with the initial speed $v = 0.17$, (c) transmission with $v = 0.171$, (d) reflectance (red dashed line) and transmittance (blue solid line) versus the initial speed of quantum droplet with $N = 10$, (e) quantum reflection of the large droplet with the initial speed $v = 0.0853$, and (f) transmission with $v = 0.086$. The other parameters are $U_0 = 25$, $\alpha = \sqrt{U_0}$, $g = 1$, and $\bar{x}_0 = -35$. Here the potential depth U_0 is very large in comparison to Fig. 2.

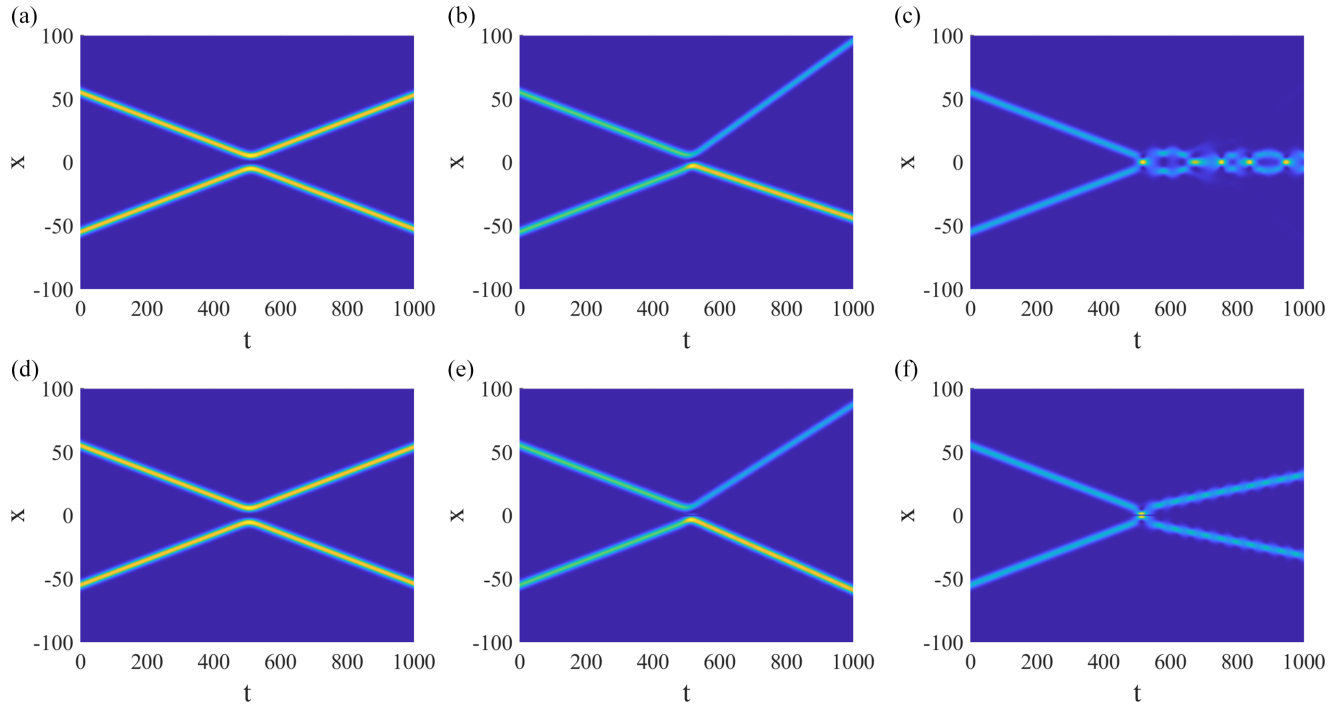


FIG. 10. (a)–(c) Collisions between two quantum droplets ($N_1 = N_2 = 1$) in free space, launched as Eq. (26), for $U_0 = 0$ and (a) $\varphi = \pi$, (b) $\varphi = 3\pi/2$ and (c) $\varphi = 0$. (d)–(f) Collisions between two quantum droplets ($N_1 = N_2 = 1$) in the presence of reflectionless potential well centered at $x = 0$ for $U_0 = 4$ and (d) $\varphi = 0$, (e) $\varphi = \pi/2$, and (f) $\varphi = \pi$. In these figures, $v = 0.1$ is fixed.

the trapped mode cannot be correctly captured by the trial function used in the variational method. For small quantum droplets, the condition $\omega_\eta < -\mu$ is marginally satisfied, i.e., only the breathing mode exists below the particle emission threshold. In general, when the droplet scatters from the reflectionless potential, the radiation is completely absent. This is due to the fact that the internal mode always occurs for quantum droplets. Only when the potential depth is sufficiently large can the small quantum droplets be excited to the continuum spectrum, resulting in vanishingly small emission of particles out of the droplet, as shown in the inset of Fig. 9(a). For large quantum droplets, however, more internal modes will stay below the particle emission threshold. The excitation of higher internal modes inhibits the loss of particle number, allowing the droplet to traverse the scattering region with probability one even for sufficiently large potential depths. This property of complete transmission and complete reflection is quite different from the scattering of solitons with a large number of particles, where such a large object may become radiated and be partially trapped by the potential due to the fact that the soliton width shrinks as N increases. As a matter of fact, for soliton scattering, it is impossible to completely avoid the radiation, because the 1D soliton supports no small-amplitude collective (internal) modes.

VI. COLLISIONS BETWEEN TWO DROPLETS AT THE REFLECTIONLESS POTENTIAL

Low-energy collisions of two interacting quantum droplets can cause them to merge, repel, or evaporate by manipulating the quantum phases [75]. The dynamics of interacting quantum droplets is closely related to the relative phases of

the two droplets. The scattering of quantum droplets at the reflectionless potential induces a phase change, which is expected to play an important role in the collision dynamics when the quantum droplets collide at the reflectionless potential. To probe the effect of the reflectionless potential on quantum droplet collisions, we simulated Eq. (14) using the SSF method, selecting two oppositely moving droplets as the initial condition,

$$\psi(x, 0) = e^{ivx+\varphi}\psi_1(x + \tilde{x}_0) + e^{-ivx}\psi_2(x - \tilde{x}_0), \quad (26)$$

where $\psi_1(x)$ and $\psi_2(x)$ are the stationary profiles of the quantum droplets normalized to N_1 and N_2 , respectively, taken from Eq. (3). This ansatz (26) sets two initial droplets, separated by distance $2\tilde{x}_0$, with speeds of $\pm v$ and an initial phase difference φ between them.

Figure 10 shows the density profiles of the collisions between a pair of slowly moving small droplets with equal norm ($N_1 = N_2 = 1$) and equal and opposite speed ($v = 0.1$) in free space [Figs. 10(a)–10(c)] and at the reflectionless potential centered at $x = 0$ [Figs. 10(d)–10(f)]. As illustrated in Figs. 10(a)–10(c), two small droplets colliding in the free space repel each other at $\varphi = \pi$ [Fig. 10(a)], experience mass transfer between the two droplets at $\varphi = 3\pi/2$ [Fig. 10(b)], and merge (small-amplitude repeated coalescence) at a relatively small value of v [Fig. 10(c)] or pass through each other at large v (not shown) when the initial relative phase is $\varphi = 0$. For comparison, we also explore the two small droplets colliding in the presence of a reflectionless potential, as shown in Figs. 10(d)–10(f). The comparison shows that when the initial relative phase is changed by π , the picture of the collision between two droplets with and without potential

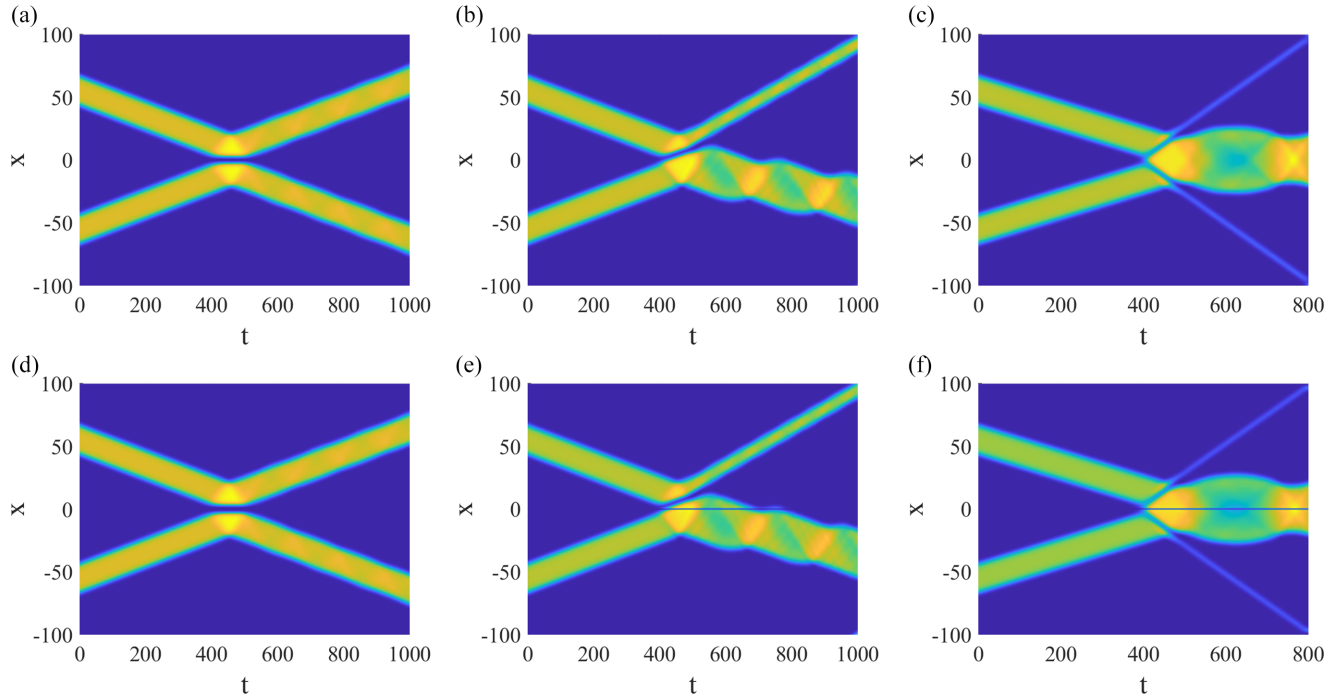


FIG. 11. (a)–(c) Collisions between two quantum droplets ($N_1 = N_2 = 10$) in free space, launched as Eq. (26), for $U_0 = 0$ and (a) $\varphi = \pi$, (b) $\varphi = 3\pi/2$, and (c) $\varphi = 0$. (d)–(f) Collisions between two quantum droplets ($N_1 = N_2 = 10$) in the presence of reflectionless potential well centered at $x = 0$ for $U_0 = 4$ and (d) $\varphi = 0$, (e) $\varphi = \pi/2$, and (f) $\varphi = \pi$. In these figures, $v = 0.1$ is fixed.

is basically the same, indicating that the phase jump acquired by the scattering plays a key role in the collisions. The only exception is that, as can be seen by comparing Figs. 10(f) and 10(c), when the speed is $v = 0.1$, the collision outcome of two small droplets of $\varphi = \pi$ with reflectionless potential is different from that of two small droplets of $\varphi = 0$ without reflectionless potential: The former pass through each other and the latter merge. However, if we vary the speed, two small out-of-phase droplets colliding in the presence of the reflectionless potential will undergo a transition from merging to passing through each other, which is the same as the collision of two small in-phase droplets in free space. These results imply that the reflectionless potential in quantum droplet collisions corresponds to a π phase difference generator.

Now we turn our attention to the case of collisions between two large quantum droplets with equal norm $N_1 = N_2 = 10$. The outcomes of the collision between two large droplets have been elaborated in Ref. [34], the distinctive features of which are this collision of such extended droplets leads to fragmentation and merger, accompanied by visible excitation of a single droplet as long as the initial phase difference is not equal to π . Comparing the results without external potential [Figs. 11(a)–11(c)] and with external potential [Figs. 11(d)–11(f)], we also observe that if we assign a π shift to the initial relative phase, the outcomes of the collisions between the two slowly moving large droplets with external potential are basically the same as those without external potential. The only difference between the cases of without potential ($\varphi = 0$) and with potential ($\varphi = \pi$) is that the presence of the reflectionless potential results in a central node in the newly formed central quiescent droplet. So far, we have dealt only with the collision of two droplets moving at a relatively low

speed. Our numerical simulations (not shown) reveal that the conclusion about the role of the phase difference generated by the reflectionless potential in the quantum droplet collisions is unaffected when we consider two fast-moving droplets. Finally, we emphasize that the effect of the initial relative phase on the collision smears out when the reflectionless potential is deep, naturally because the droplet-potential interaction rather than the droplet-droplet interaction dominates in this case.

VII. CONCLUSION

In this paper we have studied the scattering of one-dimensional binary Bose gases forming self-bound quantum droplets from a reflectionless Pöschl-Teller potential well, by solving the modified GPE with cubic (MF) and attractive quadratic (BMF) nonlinearities. Using direct numerical calculations and variational methods with a position-dependent wave function, the critical speed between quantum reflection and transmission and the corresponding trapped modes were accurately accounted for and two types of physically distinct scattering of quantum droplets were identified. The scattering of the small droplet exhibited solitonlike behavior, where a spatially symmetric trapped mode formed at the critical speed. However, the situation was quite different for large flat-top droplets: The trapped mode formed at the critical speed turned out to be the nonlinear stationary state of the system with a density profile asymmetric with respect to the center of the potential. Furthermore, we observed a nonmonotonic dependence of the critical speed on the droplet size: For small droplets, the critical speed increased with the atom number, as in the case of bright solitons, whereas for large droplets the critical speed decreased with increasing atom number.

We also investigated the collective excitations provoked by the scattering and the dynamics of the collisions between two quantum droplets in the reflectionless potential. Analysis of the small-amplitude excitation spectra showed that as the number of particles increased, the droplets supported more internal modes below the particle emission threshold, and thus excitation of higher internal modes prevented particle loss and made it easier for the droplets to pass through the scattering region without radiation. This property contrasts sharply with the scattering of solitons with a large number of particles, where such a large object may be radiated and partially trapped by the potential because the width of the solitons, unlike the large flat-top droplets, decreases with the increasing number of particles.

Before concluding, we briefly discuss the feasibility and challenges of experimental implementation of one-dimensional quantum droplet scattering. Although the dynamics of 1D droplets has been the subject of several papers [34–37,44], 1D droplets have not yet been observed experimentally. Experimentally, droplets in Bose-Bose mixtures have been observed not only in free space [2] but also in elongated cigar potentials [3], corresponding to quasi-1D situations with a 3D LYH term where the motion of particles is frozen in the tight confinement direction. In order to reach the true 1D regime, it has been theoretically suggested that ξ , which is related to the ratio of the mean-field energy to the transverse confinement energy, should be less than or equal to 0.03 [29]. Here we consider a mixture of two spin states of ^{39}K , confined in a 1D configuration with a strong radial harmonic confinement $\omega_{\perp}/2\pi = 899$ Hz. The harmonic-oscillator length is $a_{\text{HO}} = \sqrt{\hbar/m\omega_{\perp}} \approx 0.53$ μm and the relevant scattering lengths of intracomponents and intercomponents are $a_{\uparrow\uparrow} > 0$ and $a_{\downarrow\downarrow} > 0$, and $a_{\uparrow\downarrow} < 0$, respectively, associated with the 1D coupling constant $g_{\sigma\bar{\sigma}} = 2\hbar\omega_{\perp}a_{\sigma\bar{\sigma}}$. Following Ref. [27], we define $\lambda = a/a_{\text{HO}}$ and $\delta\tilde{a} = 4\delta a/[\lambda(a_{\uparrow\uparrow}^{1/2} + a_{\downarrow\downarrow}^{1/2})^2]$, where $\delta a = a_{\uparrow\downarrow} + \sqrt{a_{\uparrow\uparrow}a_{\downarrow\downarrow}}$ and $a = \sqrt{a_{\uparrow\uparrow}a_{\downarrow\downarrow}}$. For $\delta\tilde{a} \approx 1$, the pure 1D LHY term dominates in the 1D-3D crossover [27]. Considering the symmetric case $a_{\uparrow\uparrow} = a_{\downarrow\downarrow}$, the condition $\xi \leq 0.03$ requires $-a/L < \delta a/a$ [29], where $L \approx a_{\text{HO}}$ is length scale of the tight confinement. For realistic experimental parameters, $\delta\tilde{a} \approx 1$, corresponding to $\delta a/a = a/a_{\text{HO}}$, would satisfy the condition $\xi \leq 0.03$, where the pure 1D model of Ref. [30] can be applied. As an example, we take $a = 50a_0$, where a_0 is the Bohr radius, and the MF parameter δa needs to be modulated to $0.25a_0$. In our numerical simulations, the dimensionless parameter $g = \delta g/\delta g_0$ is chosen as $g = 1$ and the actual number of particles in the system is given by $\tilde{N} = \frac{2N}{\pi}(\delta g/g_0)^{-3/2} \approx 1.8N \times 10^3$. Thus, $N = 1$ corresponds to 1800 atoms. However, the experimental implementation of droplets is usually the asymmetric case where $N_{\uparrow}/N_{\downarrow} = \sqrt{g_{\downarrow\downarrow}/g_{\uparrow\uparrow}}$, but the system can still be described by a single wave function $\Psi(x)$, which

is related to the individual component wave functions by $\Psi_{\sigma}(x) = g_{\sigma\bar{\sigma}}^{1/4}\Psi(x)/\sqrt{\sqrt{g_{\sigma\sigma}} + \sqrt{g_{\bar{\sigma}\bar{\sigma}}}}$, where $\bar{\uparrow} = \downarrow$ and $\bar{\downarrow} = \uparrow$, and the evolution equation for the dimensionless $\psi(x)$ [obtained by normalizing $\Psi(x)$] has the same form as Eq. (2) [36]. In experiment, the scattering lengths as a function of the magnetic field have been explored with ^{39}K atoms and the condition $\delta a = 0$ can be satisfied at $B \approx 56.77$ G, where $a_{\uparrow\uparrow} \approx 33.5a_0$, $a_{\downarrow\downarrow} \approx 84.3a_0$, and $a_{\uparrow\downarrow} \approx -53.1a_0$ [3]. The MF parameters $\delta g = 0$ can be varied around zero by slightly adjusting the magnetic field, which may allow the unit for the norm N to be much more adjustable than in the case of the symmetric quantum droplet. It is worth noting that as one moves towards the 1D regime, the energy scale (the energy per particle) rapidly decreases to very low values, which demands extreme precision in the control of the trap parameters, such as its longitudinal flatness, and may pose a challenge for the observation of 1D quantum droplets with a purely 1D BMF effect. In addition, potential wells (barriers) can be generated by illuminating the condensate with a red (blue)-detuned laser beam, and the quantum reflection of one-dimensional bright solitons through an attractive potential was experimentally probed (see Ref. [68]), which provides the basis for our experimental investigation of the quantum reflection of 1D quantum droplets through an attractive potential. As experimental techniques continue to improve, we expect that our results will be realistically observable in future experiments on low-dimensional quantum droplets.

Finally, it should be mentioned that the steplike transition between full reflection and full transmission is a unique feature of the reflectionless potential regardless of the potential depths, as any other form of potential well with similar width and depth would generate splitting and a significant amount of radiation. An interesting direction for future work is to investigate the quantum droplet moving in a Gaussian potential or other shapes, which may exhibit a great deal of complexity in transmission-reflection properties such as partial trapping, full trapping, high-speed ejection, and so on. It is envisaged that the flat-top density profile and collective excitation would also impart some exceptional scattering properties to the quantum droplet moving in the Gaussian and other shaped potential wells.

ACKNOWLEDGMENTS

The work was supported by the National Natural Science Foundation of China (Grants No. 12375022 and No. 11975110), the Natural Science Foundation of Zhejiang Province (Grant No. LY21A050002), and Zhejiang Sci-Tech University Scientific Research Start-up Fund (Grant No. 20062318-Y). Y.G. was also supported by the National Natural Science Foundation of China (Grant No. 12275033) and the Natural Science Foundation of Hunan Province (Grant No. 2022JJ30582).

- [1] C. R. Cabrera, L. Tanzi, J. Sanz, B. Naylor, P. Thomas, P. Cheiney, and L. Tarruell, *Science* **359**, 301 (2018).
 [2] G. Semeghini, G. Ferioli, L. Masi, C. Mazzinghi, L. Wolswijk, F. Minardi, M. Modugno, G. Modugno, M. Inguscio, and M. Fattori, *Phys. Rev. Lett.* **120**, 235301 (2018).

- [3] P. Cheiney, C. R. Cabrera, J. Sanz, B. Naylor, L. Tanzi, and L. Tarruell, *Phys. Rev. Lett.* **120**, 135301 (2018).
 [4] C. D'Errico, A. Burchianti, M. Prevedelli, L. Salasnich, F. Ancilotto, M. Modugno, F. Minardi, and C. Fort, *Phys. Rev. Res.* **1**, 033155 (2019).

- [5] Z. Guo, F. Jia, L. Li, Y. Ma, J. M. Hutson, X. Cui, and D. Wang, *Phys. Rev. Res.* **3**, 033247 (2021).
- [6] M. Schmitt, M. Wenzel, F. Böttcher, I. Ferrier-Barbut, and T. Pfau, *Nature (London)* **539**, 259 (2016).
- [7] H. Kadau, M. Schmitt, M. Wenzel, C. Wink, T. Maier, I. Ferrier-Barbut, and T. Pfau, *Nature (London)* **530**, 194 (2016).
- [8] I. Ferrier-Barbut, H. Kadau, M. Schmitt, M. Wenzel, and T. Pfau, *Phys. Rev. Lett.* **116**, 215301 (2016).
- [9] L. Chomaz, S. Baier, D. Petter, M. J. Mark, F. Wächtler, L. Santos, and F. Ferlaino, *Phys. Rev. X* **6**, 041039 (2016).
- [10] I. Ferrier-Barbut, M. Wenzel, F. Böttcher, T. Langen, M. Isoard, S. Stringari, and T. Pfau, *Phys. Rev. Lett.* **120**, 160402 (2018).
- [11] F. Böttcher, J. N. Schmidt, M. Wenzel, J. Hertkorn, M. Guo, T. Langen, and T. Pfau, *Phys. Rev. X* **9**, 011051 (2019).
- [12] F. Böttcher, M. Wenzel, J. N. Schmidt, M. Guo, T. Langen, I. Ferrier-Barbut, T. Pfau, R. Bombín, J. Sánchez-Baena, J. Boronat, and F. Mazzanti, *Phys. Rev. Res.* **1**, 033088 (2019).
- [13] D. S. Petrov, *Phys. Rev. Lett.* **115**, 155302 (2015).
- [14] N. B. Jørgensen, G. M. Bruun, and J. J. Arlt, *Phys. Rev. Lett.* **121**, 173403 (2018).
- [15] T. G. Skov, M. G. Skou, N. B. Jørgensen, and J. J. Arlt, *Phys. Rev. Lett.* **126**, 230404 (2021).
- [16] T. D. Lee, K. Huang, and C. N. Yang, *Phys. Rev.* **106**, 1135 (1957).
- [17] F. Böttcher, J. N. Schmidt, J. Hertkorn, K. S. H. Ng, S. D. Graham, M. Guo, T. Langen, and T. Pfau, *Rep. Prog. Phys.* **84**, 012403 (2021).
- [18] Z. H. Luo, W. Pang, B. Liu, Y. Y. Li, and B. A. Malomed, *Front. Phys.* **16**, 32201 (2021).
- [19] L. Chomaz, I. Ferrier-Barbut, F. Ferlaino, B. Laburthe-Tolra, B. L. Lev, and T. Pfau, *Rep. Prog. Phys.* **86**, 026401 (2023).
- [20] G. Ferioli, G. Semeghini, S. Terradas-Briansó, L. Masi, M. Fattori, and M. Modugno, *Phys. Rev. Res.* **2**, 013269 (2020).
- [21] C. Fort and M. Modugno, *Appl. Sci.* **11**, 866 (2021).
- [22] A. Cappellaro, T. Macrì, and L. Salasnich, *Phys. Rev. A* **97**, 053623 (2018).
- [23] X. Cui and Y. Ma, *Phys. Rev. Res.* **3**, L012027 (2021).
- [24] V. Cikojević, L. V. Markić, G. E. Astrakharchik, and J. Boronat, *Phys. Rev. A* **99**, 023618 (2019).
- [25] N. Guebli and A. Boudjemâa, *Phys. Rev. A* **104**, 023310 (2021).
- [26] G. Ferioli, G. Semeghini, L. Masi, G. Giusti, G. Modugno, M. Inguscio, A. Gallemlí, A. Recati, and M. Fattori, *Phys. Rev. Lett.* **122**, 090401 (2019).
- [27] L. Lavoine and T. Bourdel, *Phys. Rev. A* **103**, 033312 (2021).
- [28] T. Ilg, J. Kumlin, L. Santos, D. S. Petrov, and H. P. Büchler, *Phys. Rev. A* **98**, 051604(R) (2018).
- [29] P. Zin, M. Pylak, T. Wasak, M. Gajda, and Z. Idziaszek, *Phys. Rev. A* **98**, 051603(R) (2018).
- [30] D. S. Petrov and G. E. Astrakharchik, *Phys. Rev. Lett.* **117**, 100401 (2016).
- [31] G. E. Astrakharchik and S. Giorgini, *J. Phys. B* **39**, S1 (2006).
- [32] L. Parisi and S. Giorgini, *Phys. Rev. A* **102**, 023318 (2020).
- [33] B. A. Malomed, *Front. Phys.* **16**, 22504 (2021).
- [34] G. E. Astrakharchik and B. A. Malomed, *Phys. Rev. A* **98**, 013631 (2018).
- [35] S. R. Otajonov, E. N. Tsoy, and F. K. Abdullaev, *Phys. Lett. A* **383**, 125980 (2019).
- [36] M. Tylutki, G. E. Astrakharchik, B. A. Malomed, and D. S. Petrov, *Phys. Rev. A* **101**, 051601(R) (2020).
- [37] T. Mithun, A. Maluckov, K. Kasamatsu, B. A. Malomed, and A. Khare, *Symmetry* **12**, 174 (2020).
- [38] M. R. Pathak and A. Nath, *Sci. Rep.* **12**, 6904 (2022).
- [39] I. A. Englezos, S. I. Mistakidis, and P. Schmelcher, *Phys. Rev. A* **107**, 023320 (2023).
- [40] E. Chiquillo, *Phys. Rev. A* **99**, 051601(R) (2019).
- [41] A. Tononi, Y. Wang, and L. Salasnich, *Phys. Rev. A* **99**, 063618 (2019).
- [42] S. Gangwar, R. Ravisankar, P. Muruganandam, and P. K. Mishra, *Phys. Rev. A* **106**, 063315 (2022).
- [43] T. Mithun, S. I. Mistakidis, P. Schmelcher, and P. G. Kevrekidis, *Phys. Rev. A* **104**, 033316 (2021).
- [44] A. Debnath, A. Khan, and B. A. Malomed, *Commun. Nonlinear Sci. Numer. Simul.* **126**, 107457 (2023).
- [45] F. Baronio, C. De Angelis, P. Pioger, V. Couderc, and A. Barthélémy, *Opt. Lett.* **29**, 986 (2004).
- [46] H. Friedrich and J. Trost, *Phys. Rep.* **397**, 359 (2004).
- [47] R. Coté, H. Friedrich, and J. Trost, *Phys. Rev. A* **56**, 1781 (1997).
- [48] M. Lizunova and O. Gamayun, [arXiv:2010.03385](https://arxiv.org/abs/2010.03385).
- [49] H. Sakaguchi and M. Tamura, *J. Phys. Soc. Jpn.* **74**, 292 (2005).
- [50] C. Weiss and Y. Castin, *Phys. Rev. Lett.* **102**, 010403 (2009).
- [51] A. I. Streltsov, O. E. Alon, and L. S. Cederbaum, *Phys. Rev. A* **80**, 043616 (2009).
- [52] S. D. Hansen, N. Nygaard, and K. Mølmer, *Appl. Sci.* **11**, 2294 (2021).
- [53] O. V. Marchukov, B. A. Malomed, V. A. Yurovsky, M. Olshanii, V. Dunjko, and R. G. Hulet, *Phys. Rev. A* **99**, 063623 (2019).
- [54] J. L. Helm, S. J. Rooney, C. Weiss, and S. A. Gardiner, *Phys. Rev. A* **89**, 033610 (2014).
- [55] J. Cuevas, P. G. Kevrekidis, B. A. Malomed, P. Dyke, and R. G. Hulet, *New J. Phys.* **15**, 063006 (2013).
- [56] A. E. Miroshnichenko, S. Flach, and B. Malomed, *Chaos* **13**, 874 (2003).
- [57] K. T. Stoychev, M. T. Primatarowa, and R. S. Kamburova, *Phys. Rev. E* **70**, 066622 (2004).
- [58] C. Lee and J. Brand, *Europhys. Lett.* **73**, 321 (2006).
- [59] T. Ernst and J. Brand, *Phys. Rev. A* **81**, 033614 (2010).
- [60] S. M. Al-Marzoug, S. M. Al-Amoudi, U. Al Khawaja, H. Bahlouli, and B. B. Baizakov, *Phys. Rev. E* **83**, 026603 (2011).
- [61] U. Al Khawaja, *Phys. Rev. E* **103**, 062202 (2021).
- [62] K. Forinash, M. Peyrard, and B. Malomed, *Phys. Rev. E* **49**, 3400 (1994).
- [63] X. Cao and B. Malomed, *Phys. Lett. A* **206**, 177 (1995).
- [64] D. J. Frantzeskakis, G. Theoharis, F. K. Diakonov, P. Schmelcher, and Y. S. Kivshar, *Phys. Rev. A* **66**, 053608 (2002).
- [65] R. H. Goodman, P. J. Holmes, and M. I. Weinstein, *Physica D* **192**, 215 (2004).
- [66] V. A. Brazhnyi and M. Salerno, *Phys. Rev. A* **83**, 053616 (2011).
- [67] M. O. D. Alotaibi and L. D. Carr, *J. Phys. B* **52**, 165301 (2019).
- [68] A. L. Marchant, T. P. Billam, M. M. H. Yu, A. Rakonjac, J. L. Helm, J. Polo, C. Weiss, S. A. Gardiner, and S. L. Cornish, *Phys. Rev. A* **93**, 021604(R) (2016).
- [69] A. L. Marchant, T. P. Billam, T. P. Wiles, M. M. H. Yu, S. A. Gardiner, and S. L. Cornish, *Nat. Commun.* **4**, 1865 (2013).

- [70] O. J. Wales, A. Rakonjac, T. P. Billam, J. L. Helm, S. A. Gardiner, and S. L. Cornish, *Commun Phys* **3**, 51 (2020).
- [71] M. Asad-uz-zaman and U. Al Khawaja, *Europhys. Lett.* **101**, 50008 (2013).
- [72] U. Al Khawaja, S. M. Al-Marzoug, H. Bahlouli, and Y. S. Kivshar, *Phys. Rev. A* **88**, 023830 (2013).
- [73] U. Al Khawaja and A. A. Sukhorukov, *Opt. Lett.* **40**, 2719 (2015).
- [74] J. Yang and T. I. Lakoba, *Stud. Appl. Math.* **118**, 153 (2007).
- [75] M. Pylak, F. Gampel, M. Płodzień, and M. Gajda, *Phys. Rev. Res.* **4**, 013168 (2022).